AGU PUBLICATIONS

JGR

Journal of Geophysical Research: Oceans

RESEARCH ARTICLE

10.1002/2017JC012820

Key Points:
- Three-dimensional analytical model developed including width convergence, Coriolis, and arbitrary cross-channel bathymetry
- Investigation of the effect of channel width convergence and friction on semidiurnal sea surface elevation and flow in a fjord-like basin
- Subsurface velocity maxima found when Stokes number was below 0.1 due to the dynamic depth of the basin

Supporting Information:
- Supporting Information S1

Correspondence to:
L. Ross,
lauren.ross1@maine.edu

Citation:
Ross, L., H. de Swart, E. Ensing, and A. Valle-Levinson (2017), Three-dimensional tidal flow in a fjord-like basin with converging width: An analytical model, *J. Geophys. Res. Oceans*, *122*, doi:10.1002/2017JC012820.

Received 21 FEB 2017
Accepted 21 AUG 2017
Accepted article online 25 AUG 2017

Three-dimensional tidal flow in a fjord-like basin with converging width: An analytical model

Lauren Ross[1], Huib de Swart[2], Erik Ensing[2], and Arnoldo Valle-Levinson[3]

[1]Department of Civil and Environmental Engineering, University of Maine, Orono, Maine, USA, [2]Institute for Marine and Atmospheric Research, Utrecht University, Utrecht, Netherlands, [3]Department of Civil and Coastal Engineering, University of Florida, Gainesville, Florida, USA

Abstract A three-dimensional analytical model was used to understand tidal dynamics in deep and narrow (fjord-like) basins. This model allows the width of the basin to decay exponentially with along-channel distance from the mouth. Both the length scale of exponential convergence L_b^* and the friction parameter A_v^* (vertical eddy viscosity) were the free parameters. Model results show amplification of the tidal amplitude toward the head of the basin. Amplification depends on the narrowing rate of the funnel-like width of the channel and on friction. Cross-channel variations in along-channel tidal flow are also sensitive to the friction parameter. A typical along-channel tidal flow distribution was found across the channel when the vertical eddy viscosity was characteristic of a basin with strong friction, or the Stokes number was larger than 0.1 ($St > 0.1$). Maximum along-channel tidal velocities (ranging from 0.25 to 0.5 m s^{-1} depending on width convergence strength) were located in the center of the basin and at the surface. Decreasing values of the Stokes number, $St < 0.1$, resulted in along-channel velocity maxima located near the lateral boundaries and subsurface in the middle of the channel. These tidal flow distributions were explained by a critical value of *St* and were verified with observations from Reloncavi Fjord, Chilean Patagonia yielding good agreement.

1. Introduction

Analytical models applied to semienclosed basins allow investigation of individual forcing mechanisms by isolating and examining them in a methodical way [e.g., *Murray*, 2003; *Winant*, 2007, 2008]. For example, one can study the sensitivity of flow in a semienclosed basin to changes in parameters such as friction, depth, channel length, channel width, rotation, and bathymetry. Many analytical models have been developed to study lateral variability of tidal flow in semienclosed basins, yet their focus has been on shallow systems [*Friedrichs and Hamrick*, 1996; *Huijts et al.*, 2006; *Winant*, 2007; *Huijts et al.*, 2011; *Ensing et al.*, 2015]. This study uses an analytical, exploratory model [*Murray*, 2003] to examine the asymptotic solution of shallow systems when the water depth approaches infinity, i.e., to understand the dynamics of tides in deep (fjord-like) basins.

Fjords are estuaries that have been carved through mountainous terrain by progressing glaciers. They are typically located in high latitudes and are known to have steep-sloping sides, low width/depth and width/length aspect ratios, and depths of hundreds of meters [*Valle-Levinson*, 2010]. However, riverine fjords, which are related to extinct glaciers, can be found as far south as 40°N in the United States [*Folger et al.*, 1972]. Precipitation, glacial melt, and river discharge provide fresh water to basins and create a thin, buoyant layer at the surface (<10% of the water column depth), which typically remains coherent along the fjord. Although horizontal density gradients in fjords are confined to a small fraction of the water column, they are regularly attributed as the primary drivers of residual flow [*Officer*, 1976; *Dyer*, 1997]. Currents below this upper, buoyant layer have been considered to be weak (<5 cm/s). Recent studies have shown that this classical view of fjord circulation may be oversimplifying the physics of their tidal and residual flows [*Cáceres et al.*, 2002; *Valle-Levinson et al.*, 2007; *Salcedo-Castro et al.*, 2011; *Valle-Levinson et al.*, 2014; *Schneider et al.*, 2014; *Sutherland et al.*, 2014].

The transverse structure of tidal residual flow has been studied in several fjords [*Cáceres et al.*, 2002; *Valle-Levinson et al.*, 2007, 2014]. In particular, *Valle-Levinson et al.* [2014] described a three-layer residual flow that was tidally driven with little influence from the buoyant layer (<10 m deep), indicating the importance of

understanding intratidal processes below the surface layer. However, there are not enough measurements to generalize the typical tidal circulation in fjords. This is because of the challenging field work conditions and isolated location of most fjords around the world. Field observations are therefore difficult to obtain, especially large-scale, basin-length measurements or measurements taken throughout a tidal cycle. Therefore, analytical models are useful to isolate and study tidal flow, as well as to interpret the data that may become available.

This study has two specific goals. The first is to gain fundamental understanding on amplitude and phase characteristics of sea level elevation and how it is modified by width convergence and internal friction in a narrow, deep basin. The second goal is to determine the effect of width convergence and internal friction on longitudinal and lateral flow. The hypothesis to be tested is that variations in internal friction will modify the depth at which the along-channel velocity maximum occurs in the water column. This hypothesis is based on *Prandle* [1982] and *Chen and de Swart* [2016] who both found a subsurface velocity maximum in along-channel tidal flow. *Chen and de Swart* [2016] called this subsurface maximum a "subsurface jet," which occurred if the ratio of the depth of the frictional boundary layer to the water depth was small ($\ll 1$). This study will advance the understanding of tidal flows in deep and narrow basins under well-mixed conditions, as these systems are overall scarely understood [*Valle-Levinson*, 2010]. Examples of such estuaries are systems located on the western coast of the Gulf of Maine [*Hulburt*, 1968] as well as deep-silled fjords.

A modified version of the idealized model of *Ensing et al.* [2015], who expanded on the model of *Winant* [2007] by including exponentially decaying width, is presented and discussed in order to address the objectives. The work presented here contains several new elements. First, the geometrical design of the basin in this study is similar to fjords with deep sills (representing a deep basin, $>$100 m, with narrow width, $\sim$3 km, and steep bathymetric sides). Second, the model includes two free parameters encompassing the width convergence strength and the frictional characteristics of the basin. As a proof-of-concept case, the modeled tidal flow is compared with observed tidal flow in a fjord of Chilean Patagonia.

The remaining sections are organized as follows. Section 2 describes the model equations and analytical solutions. Model results are presented in section 3, detailing along-channel variations of the tidal elevation, along-channel tidal flow, and three-dimensional tidal flow. Section 4 provides a discussion of the findings and presents a comparison of the model to the along-channel tidal current amplitude in Reloncavi Fjord located in Chilean Patagonia. Finally, section 5 contains the conclusions. All references to "friction" in the remainder of the manuscript will relate to internal friction. When bottom friction is being considered it will be so stated.

2. Model

This section provides a summary of the model equations and solutions. Supporting information gives details on the model and solution derivation. The idealized, three-dimensional analytical model presented in this study is based on the models of tidal flow presented in *Winant* [2007] and *Ensing et al.* [2015]. The model basin is of finite length in the along-channel direction with one open end in contact with the ocean (mouth of the basin) and the other end closed (head of the basin). A Cartesian coordinate system is chosen, where the x^* axis coincides with the centerline of the basin, with $x^*=0$ and $x^*=L_c^*$ denoting the positions of the mouth (seaward boundary) and head (landward boundary), respectively. The y^* axis is such that $y^*=\pm b^*/2$ denotes the sides of the basin. The z^* axis extends from the surface to the depth profile $h^*(y^*)$ (Figure 1). The width $b^*(x^*)$ is defined as an exponentially decreasing function, which gives the basin a natural, funnel-like shape, i.e.,

$$b^*(x^*)=\frac{B^*}{2}e^{-x^*/L_b^*}, \tag{1}$$

where B^* is the width of the basin at the seaward end ($x^*=0$) and L_b^* is the *e*-folding length scale. Depth along the basin is constant in the x^* direction, but has a rounded (U-shaped), rectangular deep channel in the y^* direction (cross-channel) (Figure 1). The bathymetry is therefore similar to that of many glacial-carved fjords found around the world [*Farmer and Freeland*, 1983; *Valle-Levinson et al.*, 2007; *Valle-Levinson*, 2010].

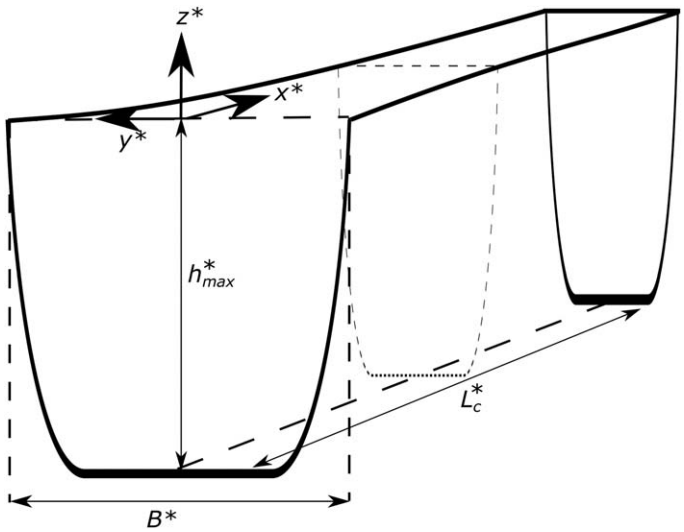

Figure 1. Diagram of the model domain with a slightly skewed cross-channel profile. The width of the channel at the seaward side is B^*, the length of the channel is L_c^*, and the maximum depth is $h_{\max}^*$. The coordinate system and origin of the x^*, y^*, and z^* axes are also shown.

The equations solved in this study include the Reynolds-averaged horizontal Navier-Stokes equations in the shallow water limit and the three-dimensional continuity equation as follows [*Csanady*, 1982; *Pond and Picard*, 1983; *Vreugdenhil*, 1994; *Pope*, 2000; *Sorenson*, 2006]:

$$\frac{\partial u^*}{\partial t^*}+u^*\frac{\partial u^*}{\partial x^*}+v^*\frac{\partial u^*}{\partial y^*}+w^*\frac{\partial u^*}{\partial z^*}-f^*v^*=-g^*\frac{\partial \eta^*}{\partial x^*}+A_v^*\frac{\partial^2 u^*}{\partial z^{*2}}, \tag{2}$$

$$\frac{\partial v^*}{\partial t^*}+u^*\frac{\partial v^*}{\partial x^*}+v^*\frac{\partial v^*}{\partial y^*}+w^*\frac{\partial v^*}{\partial z^*}+f^*u^*=-g^*\frac{\partial \eta^*}{\partial y^*}+A_v^*\frac{\partial^2 v^*}{\partial z^{*2}}, \tag{3}$$

$$\frac{\partial u^*}{\partial x^*}+\frac{\partial v^*}{\partial y^*}+\frac{\partial w^*}{\partial z^*}=0. \tag{4}$$

The along-channel, cross-channel, and vertical velocities are denoted by u^*, v^*, and w^*, respectively. The Coriolis parameter is denoted by f^*, gravitational acceleration is g^*, sea level is denoted by η^*, and the vertical eddy viscosity, which is considered constant for analytical expediency, is denoted by A_v^*. This implies that the model accounts for internal friction related to vertical shear of horizontal velocity and the source of this friction is turbulence. In the model, friction appears as the divergence of the turbulent shear stresses (or Reynolds stresses), which are simplified in terms of the product of an eddy viscosity and the vertical curvature of velocity. The maximum and average depth of the basin is denoted by $h_{\max}^*$ and $\bar{H}^*$, respectively. The density in the basin is assumed constant. This assumption is required for the model to represent only the homogeneous lower layer that encompasses the majority of the water column (>90% of the water depth) in typical fjords [*Farmer and Freeland*, 1983; *Inall and Gillibrand*, 2010; *Valle-Levinson et al.*, 2007].

The boundary conditions satisfy no stress at the surface and partial slip at the bottom. Therefore,

$$\text{at } z^*=\eta^*: \frac{\partial u^*}{\partial z^*}=\frac{\partial v^*}{\partial z^*}=0, \tag{5}$$

$$w^*=\frac{d\eta^*}{dt^*}, \tag{6}$$

$$\text{at } z^*=-h^*: A_v^*\frac{\partial u^*}{\partial z^*}=s^*u^*, \tag{7}$$

$$A_v^*\frac{\partial v^*}{\partial z^*}=s^*v^*, \tag{8}$$

$$w^* = -u^* \frac{\partial h^*}{\partial x^*} - v^* \frac{\partial h^*}{\partial y^*}, \tag{9}$$

where s^* (m s^{-1}) is the slip parameter. The transfer of horizontal momentum in the horizontal direction is ignored in equations (5), (7), and (8) and so they are approximations. In addition, there is no transport of water perpendicular to the lateral boundaries,

$$\int_{-h^*}^{\eta^*} \vec{v}^* \cdot \vec{n}\, dz^* = 0 \text{ at } y^* = -b^*(x^*)/2 \text{ and } y^* = b^*(x^*)/2, \tag{10}$$

where $\vec{v}^*$ is the velocity vector with components u^*, v^*, and $\vec{n}$ is the normal vector at the boundary. Finally, at the mouth ($x^*=0$) of the basin, the model is forced by a tide with a semidiurnal period (M_2 harmonic, 12.42 h),

$$\eta^* = Z^* \cos(\omega^* t^*) \text{ at } x^* = 0, \tag{11}$$

where ω^* is the radian frequency of the semidiurnal tide and Z^* is the tidal amplitude at the mouth. At the head of the fjord ($x^* = L_c^*$) there is no transport of water,

$$\int_{-h^*}^{\eta^*} u^* dz^* = 0 \text{ at } x^* = L_c^*. \tag{12}$$

Additional assumptions must now be made in order to adapt the equations to tidal flow in fjord-like basins.

2.1. Assumptions

Assumptions regarding the geometry and flow in the basin are expressed as nondimensional ratios. In particular, $\alpha = \frac{B^*}{L_t^*}$ is the ratio of the channel width at the mouth to the frictionless tidal wavelength, $\beta = \frac{V^*}{U^*}$ is the ratio of the cross-channel to the along-channel velocity, and $\epsilon = \frac{Z^*}{\bar{H}^*}$ is the ratio of the amplitude of the tidal wave at the open end to the average depth. The Stokes number,

$$St = \frac{2A_v^*}{\omega^* \bar{H}^{*2}}, \tag{13}$$

is the nondimensional vertical eddy viscosity [*Huijts et al.*, 2006]. In particular, St is given as the squared ratio of the thickness of the frictional bottom layer and the undisturbed water depth.

As field data suggest, in typical fjords that are long and narrow $\epsilon \ll 1$, $\alpha = \mathcal{O}(\epsilon)$ and $\beta = \mathcal{O}(\epsilon)$. The assumption that $\epsilon \ll 1$ is satisfied in a fjord because the ratio of tidal amplitude to the average depth is of the order 0.01. The assumption that $\alpha = B^*/L_t^*$ is of the order ϵ indicates that the basin is narrow (elongated). The assumption that β $(=V^*/U^*)$ is order ϵ means that the axial flow is dominant with respect to lateral flow. Typically in a fjord the magnitude of the lateral flow is approximately 10% of the magnitude of the longitudinal flow. In this work it is assumed that $\beta = 0.01$.

2.2. First-Order Equations and Solutions

Applying the appropriate scaling and assumptions (as detailed in the supporting information) to the shallow water equations (equations (2)–(4)) yields them nondimensional. Then, a regular perturbation analysis in the parameter ϵ can be applied to construct approximate solutions. We thus write,

$$u^* = u_o^* + u_1^* + \cdots, \tag{14}$$

$$v^* = v_o^* + v_1^* + \cdots, \tag{15}$$

$$w^* = w_o^* + w_1^* + \cdots, \tag{16}$$

$$\eta^* = \eta_o^* + \eta_1^* + \cdots, \tag{17}$$

where, for example, the order of magnitude of u_1^* is a factor of ϵ times the order of magnitude of u_o^*. The perturbation analysis then yields the following equations of lowest order, describing tidal flow in fjord-like basins. These equations are presented below in their dimensional form for ease of interpretation,

$$\frac{\partial u_0^*}{\partial t^*} = -g^* \frac{\partial \eta_0^*}{\partial x^*} + A_v^* \frac{\partial^2 u_0^*}{\partial z^{*2}}, \tag{18}$$

$$f^* u_0^* = -g^* \frac{\partial \eta_1^*}{\partial y^*} + A_v^* \frac{\partial^2 v_0^*}{\partial z^{*2}}, \tag{19}$$

$$\frac{\partial u_0^*}{\partial x^*} + \frac{\partial v_0^*}{\partial y^*} + \frac{\partial w_0^*}{\partial z^*} = 0. \tag{20}$$

Similarly, the first-order boundary condition equations are found as (derived from equations (5)–(12))

$$\frac{\partial u_0^*}{\partial z^*} = \frac{\partial v_0^*}{\partial z^*} = 0, \tag{21}$$

$$w_0^* = \frac{\partial \eta_0^*}{\partial t^*} \text{ at } z^* = 0; \tag{22}$$

$$A_v^* \frac{\partial u_0^*}{\partial z^*} = s^* u_0^*, \tag{23}$$

$$A_v^* \frac{\partial v_0^*}{\partial z^*} = s^* v_0^*, \tag{24}$$

$$w_0^* = -u_0^* \frac{\partial h^*}{\partial x^*} - v_0^* \frac{\partial h^*}{\partial y^*}, \text{ at } z^* = -h^*; \tag{25}$$

$$\int_{-h^*}^{0} v_0^* \, dz^* = 0 \text{ at } y^* = \pm b^*; \tag{26}$$

$$\eta_0^* = Z^* \cos \omega^* t^* \text{ at } x^* = 0; \text{ and} \tag{27}$$

$$\int_{-h^*}^{0} u_0^* \, dz^* = 0 \text{ at } x^* = L_c^*. \tag{28}$$

Solutions can be derived for the sea level height η_0^* and the horizontal and vertical velocity components u_0^*, v_0^*, and w_0^* with the lowest-order equations (18)–(20) and the appropriate lowest-order boundary conditions (equations (21)–(28)). Equations (18)–(28) are linear and the forcing is time-periodic. Thus, the solutions of the system will be of the general form

$$(u_0^*, v_0^*, w_0^*, \eta_0^*, \eta_1^*) = \mathrm{Re}[(U_0, V_0, W_0, N_0, N_1) e^{-i\omega^* t^*}], \tag{29}$$

with U_0, V_0, etc., the complex amplitudes depending on the spatial coordinates. For example, u_0^* is real and $u_0^* = |U_0| \cos(\omega^* t^* - \phi)$, where $|U_0|$ is the amplitude and ϕ is the phase. Solutions can be found for U_0, V_0, W_0, N_0, and N_1 by substituting equation (29) into the lowest-order equations and boundary conditions (equations (18)–(28)). The next-order solution for the sea surface height, N_1, is needed for the transverse momentum balance. The solution for U_0 is

$$U_0 = -\frac{i g^*}{\omega^*} \frac{dN_0}{dx^*} p_0, \tag{30}$$

where

$$p_0 = 1 - \frac{\cosh(\gamma z^*)}{\cosh(\gamma h^*) + \gamma / s^* \sinh(\gamma h^*)}, \tag{31}$$

and $\gamma = \sqrt{-i\omega^* / A_v^*}$. Equation (31) is a function of z^* but also x^* and y^* because depth also varies horizontally ($h^*(x^*, y^*)$) in a converging channel. The parameter γ^{-1} represents the thickness of the layer of frictional influence (the Stokes layer). The solution for V_0 is

$$V_0 = \frac{f^* g^*}{\omega^{*2}} \left[(p_0 - i q_0) \frac{dN_0}{dx^*} + q_0 \frac{\partial N_1}{\partial y^*} \right], \tag{32}$$

with

$$q_0 = i\gamma^2 \left[\frac{z^{*2} - 2h^*/s^* - h^{*2}}{2} \right], \tag{33}$$

and $\partial N_1/\partial y^*$ is presented in supporting information. By integrating the continuity equation (20) at lowest-order over the full depth and width, the result is

$$\frac{\partial \eta_0^*}{\partial t^*}+\frac{\partial}{\partial x^*}\int_{-h^*}^{0} u_0^*\,dz^*+\frac{\partial}{\partial y^*}\int_{-h^*}^{0} v_0^*\,dz^*=0, \tag{34}$$

and substituting equation (29) into the equation (34) we arrive at the following expression:

$$-iN_0+\frac{\partial}{\partial x^*}\int_{-h^*}^{0} U_0\,dz^*+\frac{\partial}{\partial y^*}\int_{-h^*}^{0} V_0\,dz^*=0. \tag{35}$$

Since both U_0 and V_0 are known expressions (equations (30) and (32)), equation (35) determines the solution for N_0,

$$N_0=Z^* e^{x^*/2L_b^*}\frac{\delta\cos\left[\delta/2(L_c^*-x^*)\right]+\frac{1}{L_b^*}\sin\left[\delta/2(L_c^*-x^*)\right]}{\delta\cos\left(\delta L_c^*/2\right)+\frac{1}{L_b^*}\sin\left(\delta L_c^*/2\right)}, \tag{36}$$

where

$$\delta=\sqrt{4\kappa^2-\frac{1}{L_b^{*2}}}\ \text{and}\ \kappa^2=\frac{2\omega^{*2}}{g^*}\left\langle\int_{-h^*}^{0} p_0\,dz^*\right\rangle^{-1}, \tag{37}$$

the angle brackets denote a cross-sectional mean and p_0 is as defined in equation (31), δ is the complex wavenumber of the M_2 tide, (or the tidal frequency being considered), which is a function of κ^2. The complex wavenumber δ depends on width convergence through the *e*-folding length parameter L_b^* and through p_0, which depends on h^*; it also depends on friction through γ. The above equation for N_0 (equation (36)) governs the spatial variability of the free surface. Equation (36) is the same as *Ensing et al.* [2015, equation (15)]. Two other important nondimensional parameters are

$$l=L_c^*/L_t^*\ \text{and}\ \mu=L_c^*/L_b^*, \tag{38}$$

where l is a ratio of the channel length, L_c^* to the tidal wavelength, L_t^* and μ is the ratio of the channel length to the *e*-folding length, therefore dictating the width convergence of the basin. Finally, the vertical velocity is found by integrating the continuity equation from the surface to the bottom,

$$W_0=-iN_0+\int_{z^*}^{0}\left[\frac{\partial U_0}{\partial x^*}+\frac{\partial V_0}{\partial y^*}\right]dz^{*\prime}. \tag{39}$$

The dimensionless parameters that control the solutions are the Stokes number *St* (equation (13)) as well as μ (equation (38)), δ (equation (37)), and the ratio of the Coriolis frequency to the tidal radian frequency f^*/ω^*. The results of the solutions for N_0, U_0, V_0, and W_0 are presented in section 3.

2.3. Design of Experiments

This general theoretical study aims to gain fundamental knowledge of how friction and width convergence affect tides and tidal flow in deep and narrow basins. To accomplish this goal, we chose a deep and narrow basin with a deep sill to motivate this study. In particular, Reloncavi Fjord in Chilean Patagonia was chosen because its dimensions are typical of deep and narrow basins and because data were available from this system for comparison with the model. All parameter values used in the model were taken from this system with the exception of the vertical eddy viscosity A_v^* and the *e*-folding length L_b^*, which were left as free parameters (all parameters used are shown in Table 1). This section describes the prototype system and the data collected. It then describes the sensitivity study designed to understand how tidal elevation and flow are affected by varying width convergence and friction in the fjord-like basin.

2.3.1. Prototype System: Reloncavi Fjord

Reloncavi Fjord is one of the most equatorward fjords in the world, centered at 41.6°S [*Valle-Levinson et al.*, 2007] (Figure 2). The fjord is 55 km long (L_c^*=55 km) and 3 km at the widest section (B^*=3 km). The fjord bends to the north from the mouth to the head, with the primary shift in orientation occurring approximately half way into the fjord (~27 km). The *e*-folding length of the fjord is L_b^*=137.5 km, indicating that the width convergence is slight ($\mu=L_c^*/L_b^*$=0.4). The depth ranges from a maximum of approximately h^*_{max} =400 m near the open ocean to <100 m in the most upstream portions. The average depth of the fjord is

Table 1. Model Parameter Values Representative of Reloncavi Fjord in Chilean Patagonia

Parameter	Symbol	Value
Maximum water depth	h^*_{max}	400 m
Average water depth	$\bar{H}^*$	170 m
Width at mouth	B^*	3 km
Fjord length	L^*_c	55 km
Width convergence length of Reloncavi Fjord	$L^*_{b_R}$	137.5 km
Width convergence length variations	L^*_b	$L^*_c/2=27.5$ km to $4L^*_c=220$ km
Frictionless M_2 tidal wavelength divided by 2π	L^*_t	1825 km
Amplitude of M_2 tidal elevation at the seaward end	Z^*	1 m
Angular frequency of the M_2 tidal component	ω^*	1.41×10^{-6} s^{-1}
Gravitational acceleration	g^*	9.81 m s^{-1}
Coriolis parameter	f^*	-9.57×10^{-5} s^{-1}
Vertical eddy viscosity variations	A^*_v	10^{-5} to 10^{-1} m^2 s^{-1}
Ratio of amplitude of tidal wave to the maximum depth	ϵ	0.01
Slip parameter at reference depth	s^*	10^{-5}m s^{-2}

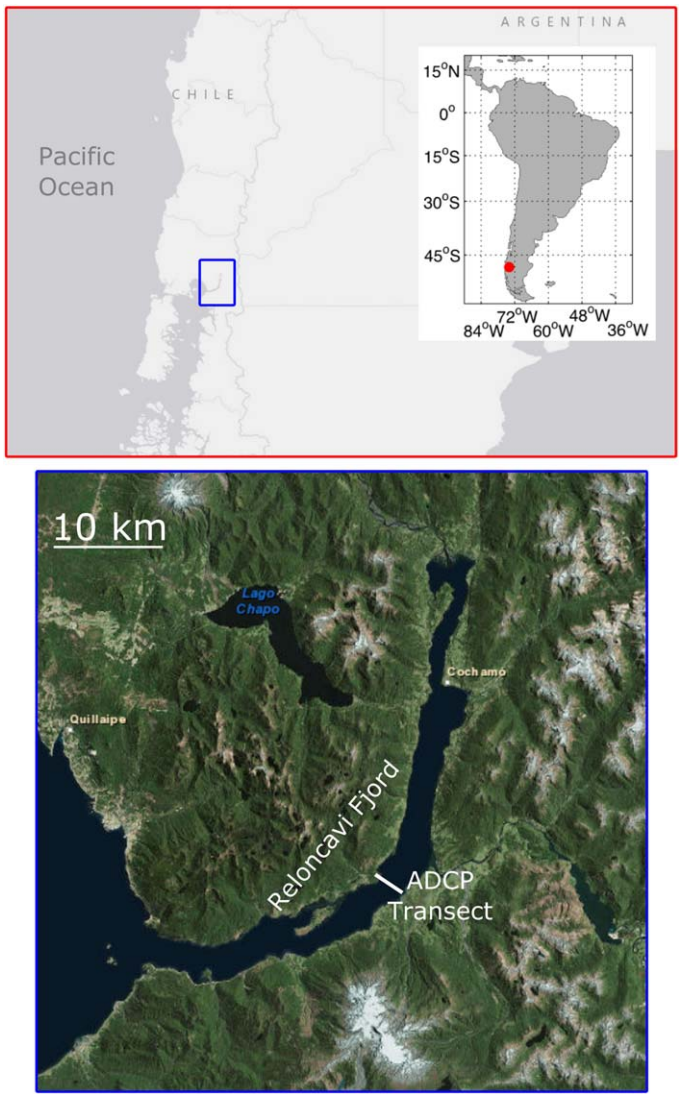

Figure 2. Location of Reloncavi Fjord in terms of Chile, and a zoom of Reloncavi Fjrod showing the location of the ADCP transect where the data were collected. Map data: Google, CNES/Airbus, US Dept of State Geographer, DigitalGlobe.

$\bar{H}^*=170$ m from the mouth to the head [*Valle-Levinson et al.*, 2007]. The tide is primarily semidiurnal with an amplitude of $Z^*=1$ m at the mouth of the fjord. The majority of the cross-sectional depth profiles of Reloncavi show broad areas of maximum depth with steep sloping sides [*Valle-Levinson et al.*, 2007]. The cross-channel depth profile used to represent that of Reloncavi Fjord is a rounded, rectangular profile (U-shape), and is given by $h^*(y^*)=[0.01+0.99(1-(y^*/b^*)^6)]h^*_{max}$ as seen in Figure 1. Table 1 details the values representative for this fjord and used in the model.

Acoustic Doppler Current Profiler (ADCP) transects were sampled on 5 May 2004 in order to obtain lateral variations of along-channel current velocities throughout a semidiurnal tidal cycle in Reloncavi Fjord. The transect extended for 2 km (cross-fjord) and occupied the midreaches of the basin (~27 km downstream). The exact location is shown in Figure 2. The current velocity measurements were collected underway with a 307.2 kHz RDI ADCP. Measurements were collected in 2 m bins every 2 s and averaged in 30 s intervals to obtain a spatial resolution of 60–75 m. Further details on the data collection are found in *Valle-Levinson et al.* [2007].

2.3.2. Sensitivity Study: Varying A^*_v and L^*_b

First, the sensitivity of water level elevation to friction and width convergence will be analyzed in order to address the first goal of this study. For this, varying *e*-folding length scales ($\mu=L^*_c/L^*_b$) representative of weak to strong width convergence will be used to calculate the water level elevation along the basin (from $x^*/L^*_c=0$ to $x^*/L^*_c=1$). Next, water level elevation will be examined as a function of *e*-folding length and friction. This will address the second goal of the study, which is assessing the impact of friction and width convergence on tidal

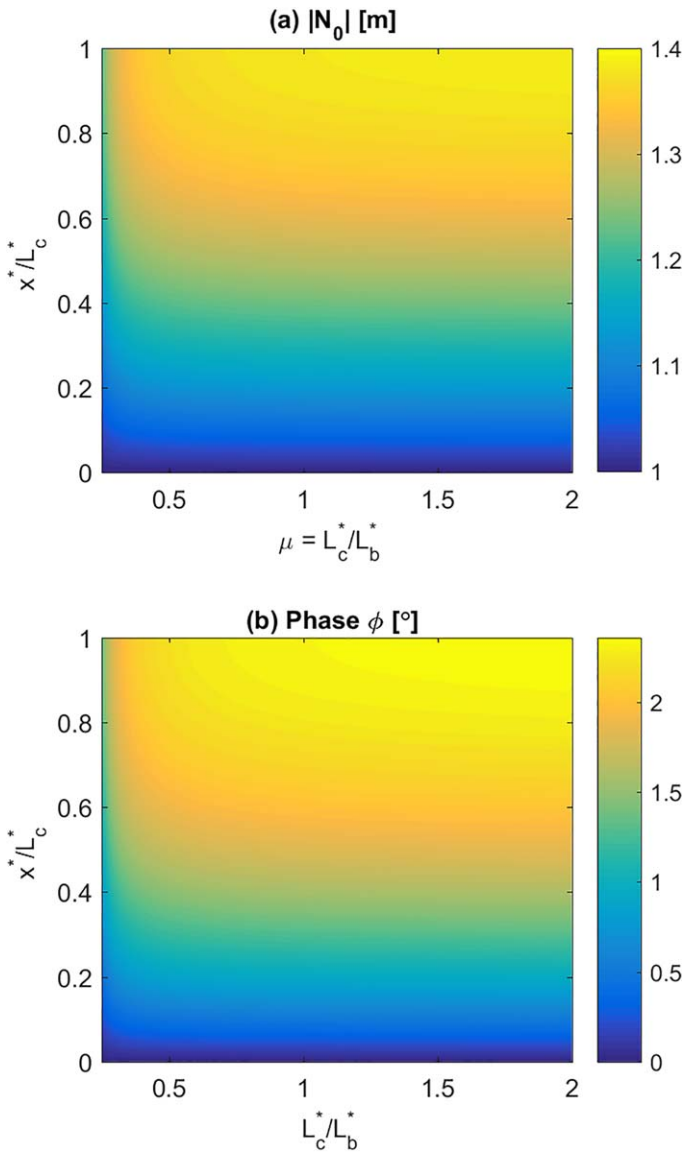

Figure 3. (a) The amplitude $|N_0|$ of the M_2 tidal elevation as a function of the ratio μ between channel length (L_c^*) and *e*-folding length scale of width convergence (L_b^*) and the along channel distance (x^*/L_c^*). The Stokes number ($St = 2A_v^*/\omega^* H_{max}^{*2}$) was set to $St = 0.031$. For the Stokes number, A_v^* is the eddy viscosity, ω^* is the angular frequency, and H_{max}^* is maximum depth. A Stokes number of 0.031 arrives when the vertical eddy viscosity is set to $A_v^* = 10^{-3}$ m^2 s^{-1}. (b) Same as Figure 3a for the phase, denoted as ϕ, of the M_2 tidal elevation.

flow. Both the tidal flow amplitude and phase, and the intratidal flow variations will be examined. The magnitude and phase of the M_2 tidal current amplitude are analyzed as a function of dimensionless cross-channel distance (y^*/B^*) and depth (z^*/h_{max}^*). The cross section was taken in the middle of the basin ($x^*/L_c^* = 1/2$) while the *e*-folding length and vertical eddy viscosity values were varied. The same procedure is carried out for the intratidal flow except that this analysis also includes the flow at various times throughout a tidal cycle. The hypothesis to be tested is that decreasing friction, in terms of the Stokes number (*St*; equation (13)) and L_b^*/L_c^* in the basin, will modify the lateral distribution of the along-channel velocity maximum independent of width convergence strength. The results of the experiments are discussed in the following section.

3. Results

Model results are presented for the amplitude of the M_2 tidal elevation and phase as well as the along-channel tidal flow for different scenarios involving the free parameters L_b^* and A_v^*. Water level elevation results will be presented first, followed by the magnitude and phase of the along-channel velocity for varying values of the vertical eddy viscosity ($A_v^* = 10^{-5}$ m^2 s^{-1} and $A_v^* = 10^{-1}$ m^2 s^{-1}; representative of a weakly and strongly frictional fjord basin, respectively) and *e*-folding length scales ($L_b^* = 4L_c^*$ to $L_c^*/2$, depicting weak, or minimal width convergence, to extreme funnel-like width convergence). This means values of the Stokes number (equation (13)) vary between 0.0003 and 3.1 and values of μ (equation (38)) vary between 0.25 and 2. All other parameter values were taken from Reloncavi Fjord and are shown in Table 1. Next, the M_2 tidal velocity will be examined for varying *e*-folding lengths and values of friction (same as those mentioned above) half-way into the basin ($x^* = L_c^*/2$).

3.1. Sea Surface Elevation

Solutions for the M_2 tidal water level amplitude ($|N_0|$) along the channel with varying *e*-folding length scales ($\mu = L_c^*/L_b^*$) are shown in Figure 3a. The vertical eddy viscosity used was $A_v^* = 10^{-3}$ m^2 s^{-1}, corresponding to a Stokes Number of $St = 0.031$. With decreasing values of L_b^* (increasing values of μ) the channel converges more rapidly, and the sea level amplifies from the mouth of the basin ($x^* = 0$) to the head ($x^* = L_c^*$) by

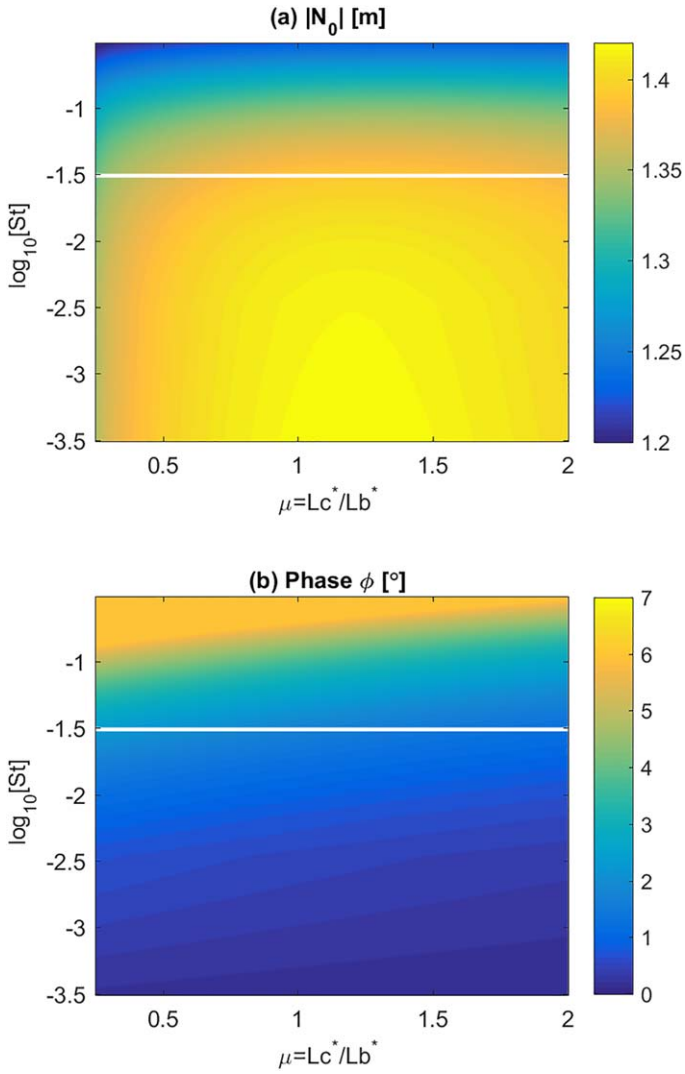

Figure 4. (a) The amplitude $|N_0|$ of the M_2 tidal elevation as a function of the ratio μ between channel length (L_c^*) and *e*-folding length scale of width convergence (L_b^*) and of $\log_{10}$ of the Stokes number ($St=2A_v^*/\omega^* H_{max}^{*2}$) at the landward end of the basin ($x^*=L_c^*$). (b) Same as Figure 4a for the phase ϕ of the M_2 tidal elevation. The white line indicates a Stokes Number of $St=0.031$, and is the same as the top horizontal line of ($x^*/L_c^*=1$) Figure 3.

approximately 0.4 m for the greatest width convergence ($\mu=2$; $L_b^*=L_c^*/2$). As $\mu \rightarrow 0$ there is little or no attenuation in the basin, implying that the basin is approaching a rectangular shape. The phase of N_0 denoted as ϕ (Figure 3b) shows a slight increase from the mouth to the head of the basin (approximately 2.5° for $\mu=2$, strong width convergence), indicating that the tidal wave behaves as a standing wave regardless of the strength of the width convergence. The dependence of the free surface elevation on varying friction (Stokes number) is now investigated at the head of the basin.

The amplitude of the M_2 tidal elevation, $|N_0|$, at the head of the basin ($x^*=L_c^*$) may amplify or attenuate. Emphasis is placed on the dependence of $|N_0|$ on the strength of channel width convergence ($L_b^*=L_c^*/2$ to $4L_c^*$; or $\mu=0.25$ to 2) and friction ($A_v^*=10^{-5}$ to $A_v^*=10^{-1}$ m^2 s^{-1} or Stokes numbers ranging from $St=0.0003$ to 3.1). Values of $|N_0|$ at the head of the basin showed increased amplification with decreasing friction for all variations of L_b^* (Figure 4a). However, strongest amplification of $|N_0|$ (~0.45 m) was found for low Stokes numbers ($St=0.03$ to 0.32) and when $1<\mu<1.5$ ($2L_c^*/3<L_b^*<L_c^*$), indicating that when width convergence is very strong in the fjord ($\mu>1.5$ or $L_b^*<2L_c^*/3$), the degree of amplification of $|N_0|$ is less pronounced (~0.35 m).

When friction increased, amplification of the sea level decreased drastically even for the strongest width convergence case, which only allowed for slight amplification of the tidal wave from the mouth to the head of the channel. For example, when $\mu=1.25$ ($L_b^*=4L_c^*/5$) the sea level amplified by ~0.5 m when friction was small ($A_v^*=10^{-5}$ m^2 s^{-1}) and only by 0.2 m when friction increased ($A_v^*>10^{-1}$ m^2 s^{-1}). The phase increased with increasing friction for all values of μ, indicating the transition of the tidal wave from standing to progressive. The most pronounced phase lag (phase lag of ~6°) occurred when channel width convergence was weak ($\mu=0.25$ or $L_b^*=4L_c^*$; Figure 4b). It should be emphasized that Figure 4 differs from Figure 3 in that Figure 4 focuses on the tidal elevation at the head of the basin ($x^*=L_c^*$) and how it varies with width convergence strength and friction (Stokes number) while Figure 3 describes how the tidal water level varies because of width convergence strength along the channel (from $x^*=0$ to L_c^*).

To confirm that the tidal wave behaves as a standing wave, the axial (from $x^*=0$ to $x^*=55$ km) phase difference between the water level ϕ_{N_0} and the along-channel velocity ϕ_{U_0} is investigated for various *e*-folding

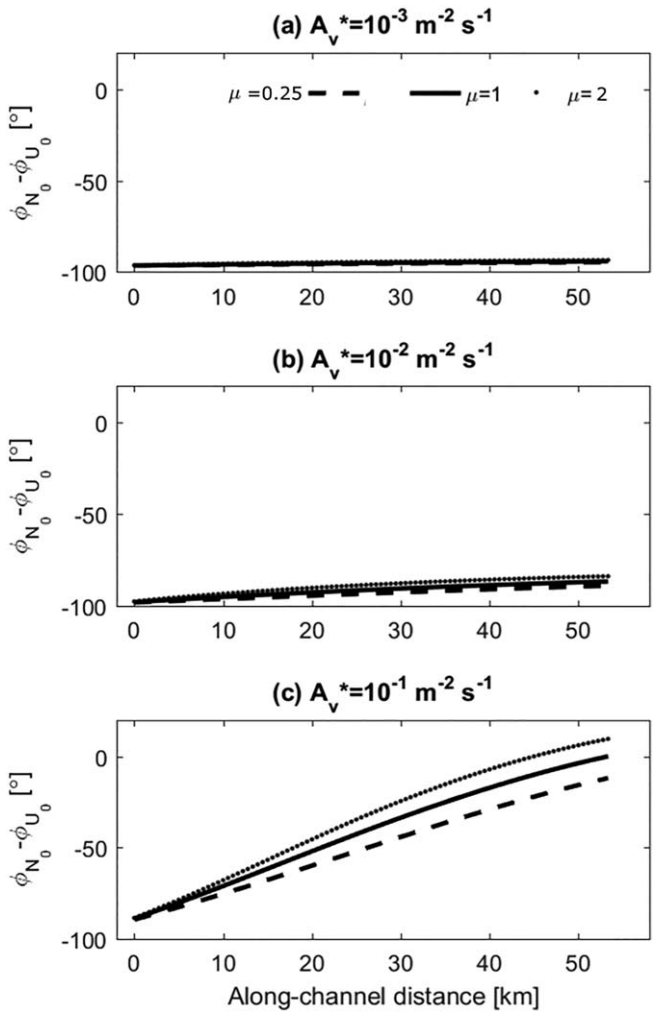

Figure 5. (a) The axial (from $x^*=0$ to $x^*=55$ km) phase difference between the sea level ϕ_{N_0} and the along-channel velocity ϕ_{U_0} for a Stokes number of 0.031, which corresponds to a vertical eddy viscosity value of $A_v^*=10^{-3}$ m^2 s^{-1}. The phase difference was calculated for $\mu=2$ ($L_b^*=L_c^*/2$, strong width convergence, depicted by dotted line), $\mu=1$ ($L_b^*=L_c^*$, moderate width convergence, depicted by the solid line), and μ=0.25 ($L_b^*=4L_c^*$, weak width convergence, depicted by the dashed line). (b) Same as Figure 5a for a Stokes number of 0.31, which corresponds to a vertical eddy viscosity value of $A_v^*=10^{-2}$ m^2 s^{-1}. (c) Same as Figure 5a for a Stokes number of 3.1, which corresponds to a vertical eddy viscosity value of $A_v^*=10^{-1}$ m^2 s^{-1}.

lengths and values of the Stokes number (Figure 5). For the case of moderate friction ($St=0.031$, $A_v^*=10^{-3}$ m^2 s^{-1}) the phase difference from the mouth ($x^*=0$ km) to the head ($x^*=55$ km) is negligible (<2°) for strong ($\mu=2$ or $L_b^*=L_c^*/2$), moderate ($\mu=1$ or $L_b^*=L_c^*$), and weak (μ=0.25 or $L_b^*=4L_c^*$) width convergence (Figure 5a). This reinforces that the tidal behavior seen in Figure 3 indeed represents a standing wave. When internal friction is augmented ($St=0.31$, $A_v^*=10^{-2}$ m^2 s^{-1}), the phase increases only slightly (<12° from mouth to head) for each of the width convergence cases, indicating that the tidal wave behaves partially as a standing wave (Figure 5b). Only when internal friction is strong ($St=3.1$, $A_v^*=10^{-1}$ m^2 s^{-1}) does the tidal wave become a progressive wave, with the phase difference starting at ~−90° at the mouth, increasing to ~0° at the head (Figure 5c). The most pronounced phase difference is for the strong width convergence case ($\mu=2$ or $L_b^*=L_c^*/2$). Further explanation on why the phase difference increases for strong friction will be provided in the discussion section. Now the amplitude of the along-channel tidal velocity will be discussed.

3.2. Amplitude of the M_2 Along-Channel Tidal Velocity

The effects of friction and width convergence on the lateral distribution of the tidal current amplitude are explored in this subsection. Two friction cases will be considered ($A_v^*=10^{-1}$ m^2 s^{-1} and $A_v^*=10^{-3}$ m^2 s^{-1}; corresponding Stokes numbers are $St=3.1$ and $St=0.03$). Each of these cases will be shown for three *e*-folding length scales, from values of L_b^* representing weak width convergence ($L_b^*=4L_c^*$ or μ=0.25) to a small L_b^* representing strong width convergence ($L_b^*=L_c^*/2$ or $\mu=2$). The location chosen for examining lateral distributions was the middle of the basin ($x^*=L_c^*/2$).

The magnitude of the along-channel velocity for the first case ($A_v^*=10^{-1}$ m^2 s^{-1}) showed typical along-channel tidal current amplitudes for all width convergence scenarios (Figure 6). Maximum flow reached 0.5 m s^{-1} in the center of the channel ($y^*/B^*=0$) and decreased to zero at the boundaries of the basin when width convergence was strong (Figure 6a). The phase showed a lag of 60° or approximately 2 h from the lateral boundaries ($y^*/B^*=\pm1$) to the middle of the channel ($y^*/B^*=0$), indicating that the tide turned first at the sides of the channel and then in the center 2 h later (Figure 6d). When width convergence was moderate ($L_b^*=L_c^*$ or $\mu=1$) for the same value of A_v^*, the M_2 tidal current amplitude maintained a similar pattern to that of the strong width convergence case (Figure 6a). But overall the values were weaker (maximum of ~0.4 m s^{-1}; Figure 6b). The associated phase, shown in Figure 6e, indicated a similar phase as the strong

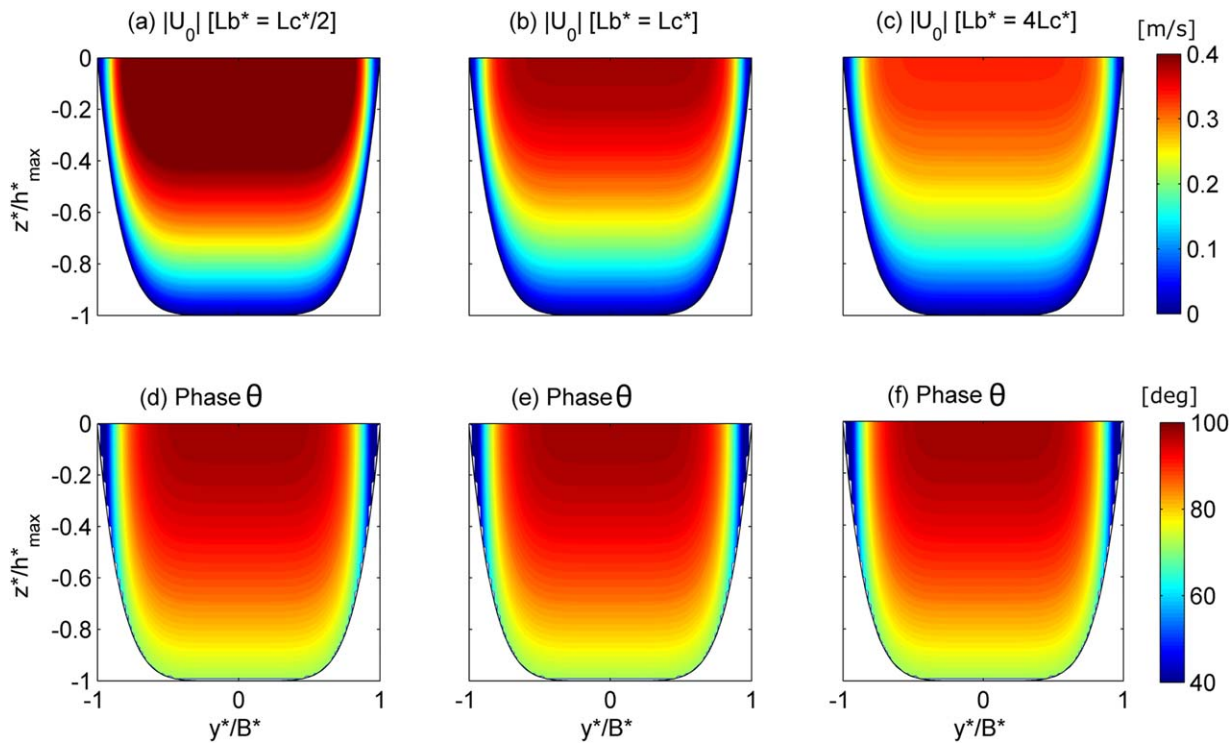

Figure 6. Along-channel M_2 tidal current amplitude $|U_0|$ as a function of cross-channel distance, y^*/B^*, and depth, z^*/h^*_{max}, for $St = 3.09$ ($A^*_v = 10^{-1}$ m^2 s^{-1}) and (a) $L^*_b = L^*_c/2$ ($\mu = 2$, strong width convergence), (b) $L^*_b = L^*_c$ ($\mu = 1$, moderate width convergence), and (c) $L^*_b = 4L^*_c$ ($\mu = 0.25$, weak width convergence). (d–f) Same as Figures 6a–6c for the phase of the along-channel M_2 tidal current magnitude, denoted as θ. All figures are taken at the center of the channel ($x^* = L^*_c/2$).

width convergence case. Finally, when width convergence was weak, minimum velocities were found (reaching only 0.3 m s^{-1}) in the center of the channel, but with the phase lag of $\sim 60^\circ$ maintained (Figures 6c and 6f).

For the second case, the vertical eddy viscosity was reduced to $A^*_v = 10^{-3}$ m^2 s^{-1}. As with the previous case (with a higher value of A^*_v), the velocity magnitude decreased with weakening width convergence of the channel, however the overall flow pattern was different than that of the first case (Figures 6 and 7). For example, for all width convergence scenarios, the maximum velocities were found at the sides of the channel ($y^*/B^* = -0.9$ and 0.9) close to the surface ($z^*/h^*_{max} > -0.2$) and also subsurface ($z^*/h^*_{max} < -0.2$) in the middle portions of the cross-section of the basin ($-0.8 < y^*/B^* < 0.8$) (Figure 7). The maximum velocity exceeded 0.5 m s^{-1} when width convergence was strong (Figure 7a). The phase change was approximately 35° from the sides and bottom of the channel toward the center indicating that the tide first turned at the boundaries and 1.5 h later turned in the center of the basin (Figure 7d). When width convergence was moderate, maximum velocities reached approximately 0.3 m s^{-1} and the phase lag was almost identical to that of the strong width convergence case (Figures 7b and 7e). Finally, when convergence was weak, $|U_0|$ diminished, only reaching approximately 0.25 m s^{-1} near the lateral boundaries. Again, the phase was similar to that of the strong and moderate width convergence cases (Figures 7c and 7f). The velocity maxima near the lateral boundaries and subsurface in the middle of the channel will be investigated further in section 4.

3.3. Intratidal Flow

The M_2 intratidal flow, as a function of channel width and depth, will now be presented for varying friction ($St = 0.03$ and 3.1) and width convergence strength ($L^*_b = L^*_c/2$ or $\mu = 2$ and $L^*_b = 4L^*_c$ or $\mu = 0.25$). All of the cross sections shown are located at the midreaches of the channel ($x^* = L^*_c/2$). Each scenario is shown for times $t^* = 0$ (high water), $t^* = T^*/8$, $t^* = T^*/4$, and $t^* = 3T^*/8$ (end of ebb).

The effect of friction on the M_2 tidal flow was investigated first for strong width convergence ($L^*_b = L^*_c/2$, $\mu = 2$). Figure 8 depicts the three-dimensional flow pattern for the eddy viscosity values described above.

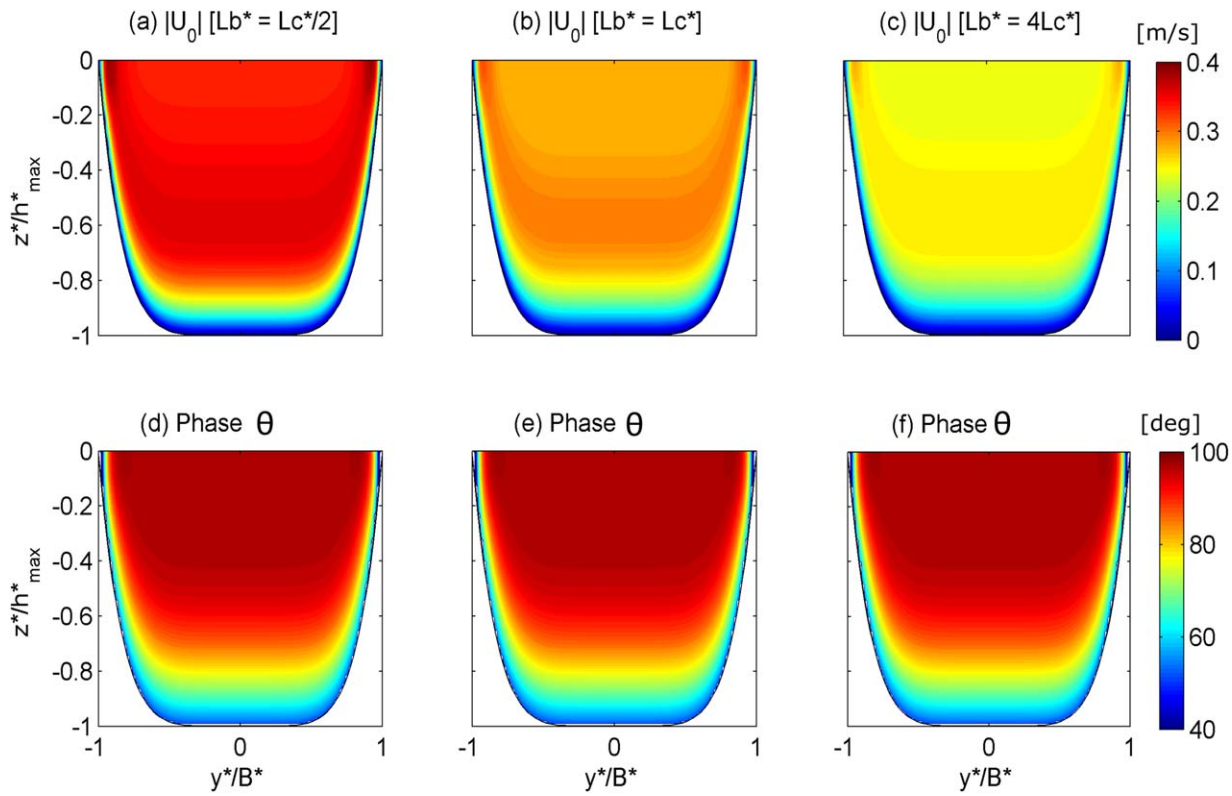

Figure 7. As Figure 6, but for $St = 0.031$ ($A_v^* = 10^{-3}$ m^2 s^{-1}).

Large Stokes numbers ($St = 3.1$; corresponding friction value of $A_v^* = 10^{-1}$ m^2 s^{-1}; Figures 8a–8d) shows strongest velocities ($u_0 = 0.15$ m s^{-1}) near the lateral boundaries at high water ($t^* = 0$; Figure 8a). A weakly developed circulation cell is apparent at this time. As the tidal cycle progresses, namely at time $t^* = T^*/4$, the location of the velocity maximum migrates to the center of the channel at the surface and reaches 0.5 m s^{-1}. The lateral and vertical velocities show flow going to the left as it enters the basin, which is indicative of Coriolis influence in the southern hemisphere (Figures 8a–8d). This pattern switches during the flood phase of the tidal cycle (not shown).

When the Stokes number was reduced to $St = 0.49$, corresponding to the vertical eddy viscosity value $A_v^* = 10^{-2}$ m^2 s^{-1}, a more pronounced circulation cell develops at high water ($t^* = 0$; Figure 8e). At all subsequent time steps ($t^* = T^*/8$, $T^*/4$, $3T^*/8$), strongest velocities are found subsurface, in particular when $-0.9 < z^*/h^*_{\max} < -0.6$ the maximum velocity is $\sim$0.25 m s^{-1} at $t^* = T^*/8$ (Figure 8f). When St is decreased further ($St = 0.03$ corresponding to the vertical eddy viscosity value $A_v^* = 10^{-3}$ m^2 s^{-1}; Figures 8i–8l), the same pattern results as that of the moderate friction case ($St = 0.31$, $A_v^* = 10^{-2}$ m^2 s^{-1}; Figures 8e–8h), except the velocity maximum is found much closer to the bottom of the channel. For example, when $t^* = T^*/4$, the velocity maximum is located in the depth range $-0.9 < z^*/h^*_{\max} < -0.8$ (Figure 8k).

Next the effect of friction on the tidal flow is considered for weak width convergence ($L_b^* = 4L_c^*$ or $\mu = 0.25$) (Figure 9). When the vertical eddy viscosity is $A_v^* = 10^{-1}$ m^2 s^{-1} ($St = 3.1$) (Figures 9a–9d), the spatial structure of the M_2 tidal flow resembles that of open channel flow, with the velocity maximum occurring at the center of the channel ($y^*/B^* = 0$) and at the surface ($z^*/h^*_{\max} = 0$) during maximum tidal velocity ($t^* = T^*/4$; Figure 9c). High water shows diminished horizontal and vertical velocities compared to that of the strong convergence case (Figures 8a and 9a). When friction is decreased to $St = 0.31$, circulation cells begin to appear during low water (Figure 9e) and along-channel velocity maxima occur near the lateral boundaries at times $t^* = 0$ and $T^*/8$ (Figures 9e and 9f). Maximum M_2 tidal velocity occurs in the center of the channel ($y^*/B^* = 0$) and at the surface ($z^*/h^*_{\max} = 0$) later in the tidal cycle ($t^* = T^*/4$ and $T^* = 3T^*/8$; Figures 9g and 9h).

Finally, when the vertical eddy viscosity was set to $A_v^* = 10^{-3}$ m^2 s^{-1}, representing a moderate friction case ($St = 0.03$), a well-defined circulation cell is apparent during high water ($t^* = 0$; Figure 9i). In addition, the

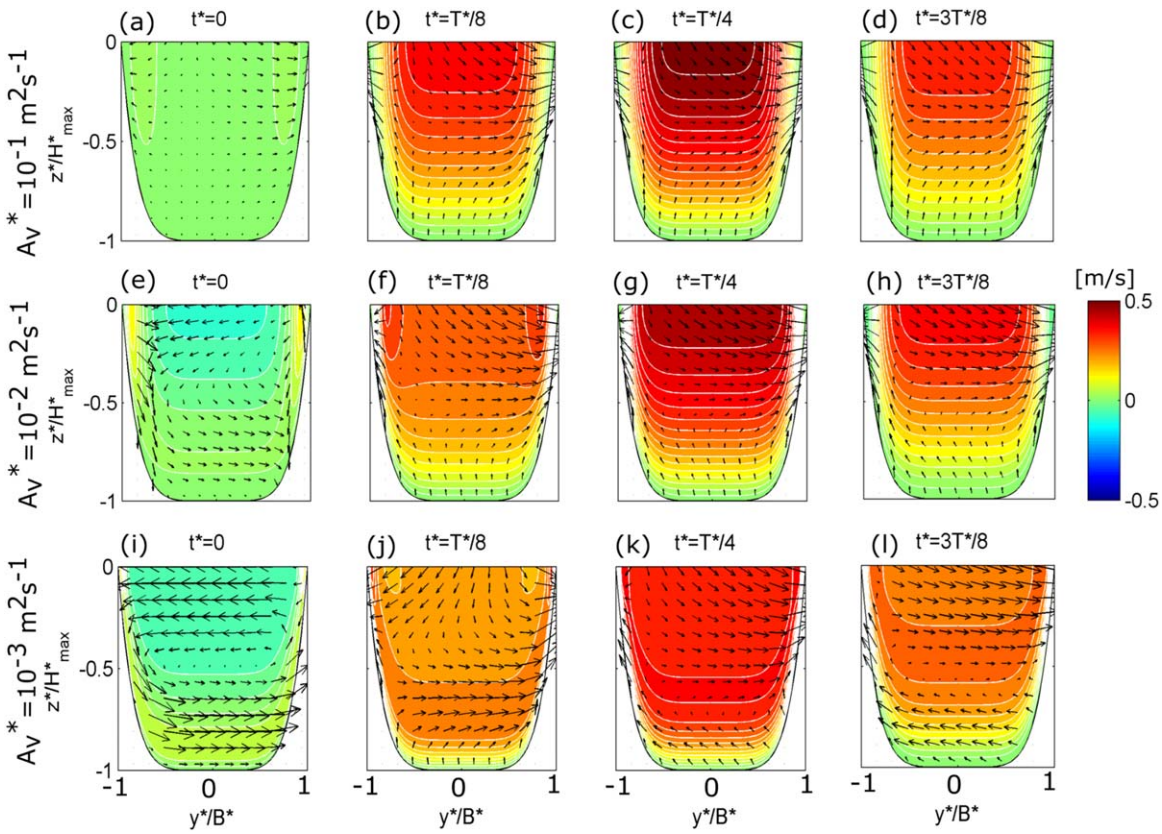

Figure 8. Colored contours represent along-channel M_2 tidal velocities and arrows represent lateral and vertical M_2 tidal velocities at $x^*=L_c^*/2$ as a function of y^*/B^* and z^*/h^*_{max} for strong width convergence, $\mu = 2$ ($L_b^*=L_c^*/2$). (a) High water or $t^*=0$, (b) $t^*=T^*/8$, (c) $t^*=T^*/4$, and (d) end of ebb or $t^*=3T^*/8$ with $St = 3.09$ ($A_v^*=10^{-1}$ m^2 s^{-1}). (e–h) Same as Figures 8a–8d with $St = 0.31$ ($A_v^*=10^{-2}$ m^2 s^{-1}). (i–l) Same as Figures 8a–8d with $St = 0.031$ ($A_v^*=10^{-3}$ m^2 s^{-1}).

along-channel velocity maxima are found near the lateral boundaries ($y^*/B^* < -0.8$ and >0.8, at the surface) and subsurface (e.g., $-0.6 < z^*/h^*_{max} < -0.3$; Figure 9l).

4. Discussion

This section explores the effect of friction on the spatial variability of the along-channel M_2 tidal velocity patterns in the basin. In particular, it addresses the processes causing the tidal velocity maxima found subsurface and near the lateral boundaries when friction decreases. The section continues with a proof-of-concept case that involves a comparison of model results to data acquired in Reloncavi Fjord and extrapolates the findings to other similar systems. Finally, the section ends with a discussion of the limitations of the model, on the basis of its geometric simplicity and other assumptions.

4.1. Effects of Friction on Along-Channel Flow

Lamb [1932] and *Prandle* [1982] showed that in homogeneous waters (unstratified), a maximum in tidal current amplitude would occur subsurface when the depth of the frictional boundary layer is much less than the water depth. They noted that this would develop in water depths exceeding 100 m. The model used in this study is designed after a fjord with maximum depth of 400 m and constant density, therefore the theoretical work described by *Prandle* [1982] is applicable in this case. The work described by *Prandle* [1982] and in this study represents basins that are dynamically deep. But the control parameter is the geometric depth of the system and not the stratification, as was the case in *Chen and de Swart* [2016], who studied tides in shallow, but stratified systems (their control parameter is h_b^*/h^* where h_b^* is the depth of the frictional layer). The occurrence of the submerged "subsurface jet" (or submerged along-channel tidal velocity maximum) in *Chen and de Swart* [2016] is therefore representative of a basin that is dynamically deep as stratification

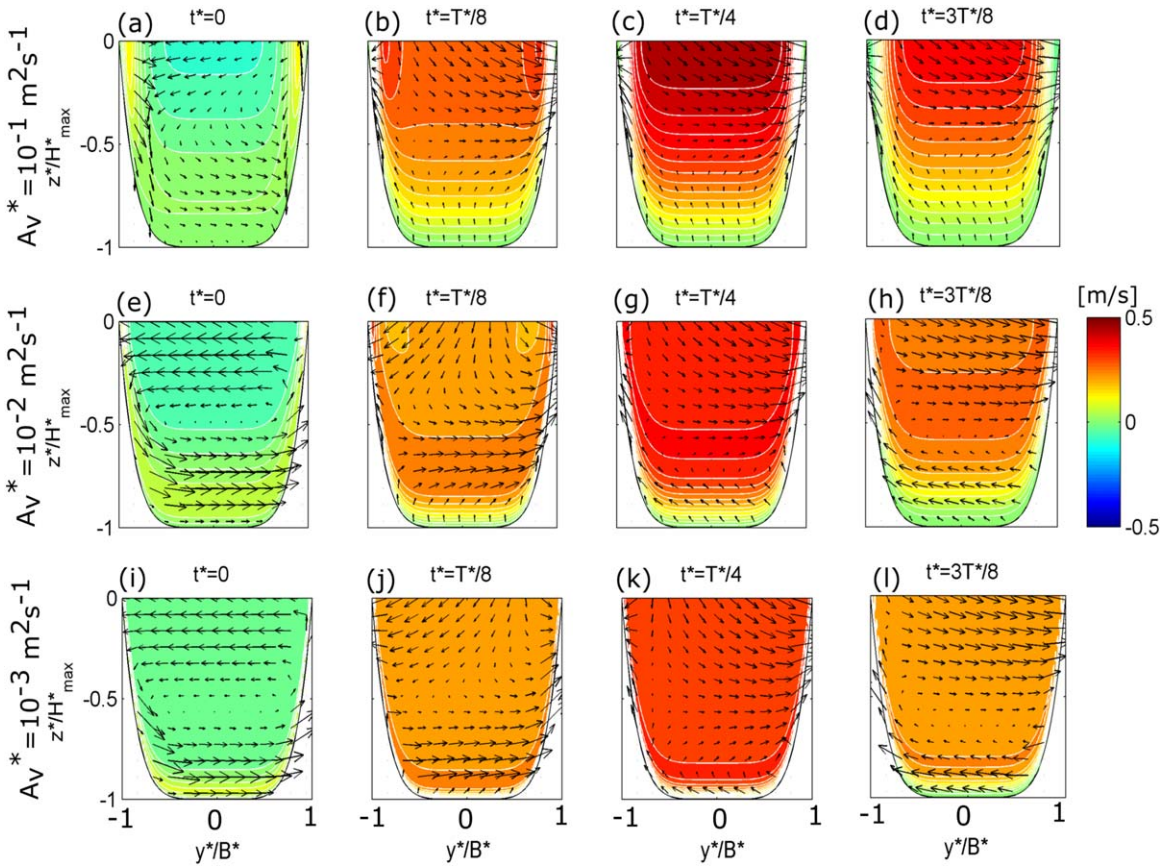

Figure 9. As Figure 7, but for weak width convergence μ=0.25 (L_b^*=4L_c^*).

suppresses mixing. This implies that although deep, unstratified basins may be morphologically different from shallow, stratified estuaries, the fundamental physics governing tidal flow is similar.

This study revealed that variations in the Stokes number influenced the location of the along-channel tidal velocity maxima as in *Prandle* [1982] and *Chen and de Swart* [2016] (Figures 6 and 7). When St= 3.1 (A_v^*= 10^{-1} m^2 s^{-1}), representative of a highly frictional basin, the along-channel M_2 velocity maximum appeared in the center of the channel and at the surface, as in open channel flow (Figures 6, 8a–8d, and 9a–9d). However, when the Stokes number decreased to St = 0.31 and 0.03 (A_v^*= 10^{-2} m^2 s^{-1} and 10^{-3} m^2 s^{-1}, respectively), the location of the along-channel velocity maximum changed (Figures 7, 8e–8l, and 9e–9l).

To further explore this response to frictional effects, the M_2 tidal current amplitude maximum was extracted from the model results at the center (y^*/B^*=0) and the midreach (x^*=$L_c^*/2$) of the basin (Figure 10a). The maximum was found for varying the Stokes number from St = 0.0003 to 4.91 and varying channel width convergence (L_b^*= 4L_c^* to $L_c^*/2$ or μ= 0.25 to 2). The M_2 tidal current amplitude showed maxima varying for different width convergence strength of the channel. The strongest along-channel velocity amplitudes ($|U_0| > 0.4$ m s^{-1}) were found for strong width convergence (L_b^*= $L_c^*/2$ or μ =2) and $St > 0.1$ ($\log_{10}(St) > -1$; Figure 10a). For example, when $St > 0.1$ and width convergence was strong (L_b^*= $L_c^*/2$), the along-channel velocity magnitude increased from 0.4 to 0.52 m s^{-1}. When $St < 0.1$ ($\log_{10}(St) < -1$), the amplitude increased from 0.32 to 0.4 m s^{-1} (Figure 10a). This indicates that St = 0.1 is a critical Stokes number, which represents a shift in the value of the along-channel tidal velocity maxima. A general expression for what values of the Stokes number will ensure a tidal velocity maximum at the surface is $St \geq (6.6\times10^{-2})/(\omega^*\bar{H}^{*2})$.

The depth of the maximum M_2 tidal current amplitude for various eddy viscosity values also provided revealing information (Figure 10b). Regardless of width convergence strength, the value of St = 0.1 (or St= $-6.6\times10^{-2}/(\omega^*\bar{H}^{*2})$) separated the location (in terms of depth) of the along-channel flow maximum. In

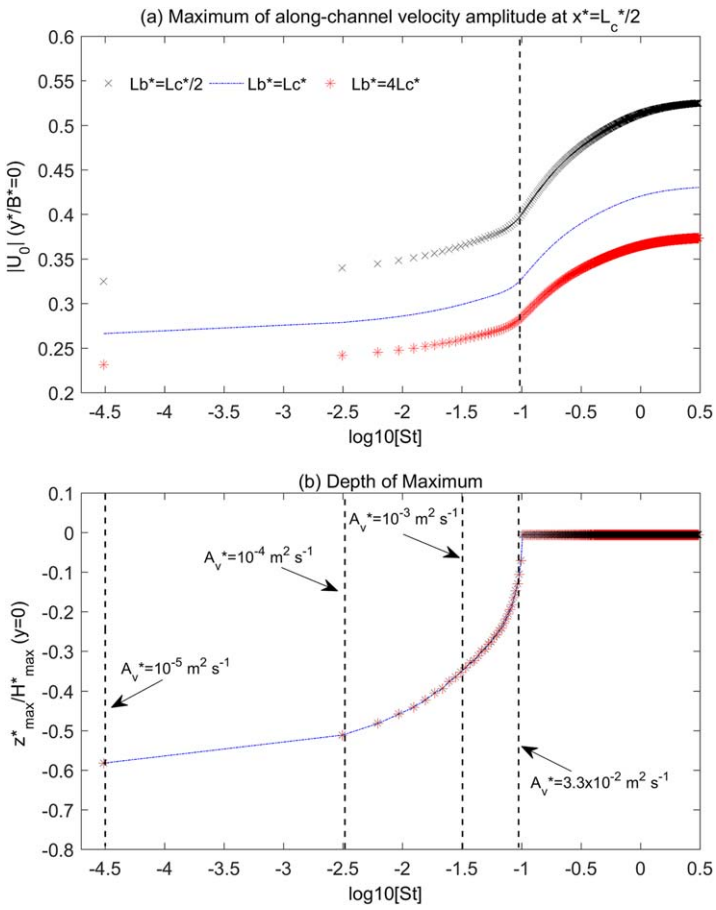

Figure 10. The (a) maximum along-channel M_2 tidal current amplitude is plotted as a function of the Stokes number ($St=2A_v^*/\omega^* H_{\max}^{*2}$) for various *e*-folding length scales $L_b^*=L_c^*/2$, $L_b^*=L_c^*$, and $L_b^*=4L_c^*$ corresponding to $\mu=2$, $\mu=1$, and $\mu=0.25$, respectively. (b) The depth of the maximum M_2 along-channel velocity amplitude (found in Figure 10a) is plotted as $\log_{10}(St)$ (for the same *e*-folding length scales as Figure 10a). Both figures represent results in the middle of the channel ($y^*/B^*=0$) half way into the basin ($x^*=L_c^*/2$).

particular, when $St>0.1$, the location of the along-channel velocity magnitude maximum was at the surface. However, when $St<0.1$, the location of the maximum migrated subsurface. As mentioned before, the Stokes number is the squared ratio of the thickness of the frictional bottom layer and the undisturbed water depth. Therefore, as values of the Stokes number decreased, the location of the velocity maximum monotonically decreased in the water column. For example, when $St=0.03$ ($A_v^*=10^{-3}$ m^2 s^{-1}), the depth of the velocity maximum occurred at $z^*/h_{\max}^*=-0.36$, but when $St=0.0003$ ($A_v^*=10^{-5}$ m^2 s^{-1}), the depth of the maximum became $z^*/h_{\max}^*=-0.59$ (Figure 10b).

The subsurface maximum in $|U_0|$ can be explained by exploring the structure of the function p_0 (equation (31)), which determines its vertical structure (equation (30)). In particular, p_0 contains the parameter $\gamma=-\sqrt{i\omega^*/A_v^*}$, which can also be expressed as $\gamma=(1-i)/\delta_E$, where $\delta_E=\sqrt{2A_v^*/\omega^*\bar{H}^{*2}}$ is the thickness of the Stokes boundary layer (analogous to the Ekman depth if $\omega^*=f^*$). Considering the situation when friction is large (i.e., $St>0.1$ so δ_E is large) p_0 simplifies, through Taylor series expansion, to $p_0=-1/2\gamma^2(z^{*2}-h^{*2}-h^*/s)$, which only has a maximum at $z^*=0$ (the surface). Therefore, the vertical structure of $|p_0|$ ensures that the depth of maximum $|U_0|$ is at the surface when $St>0.1$ (Figure 10b). However, when $St<0.1$, no such simplification can be made for p_0 and a subsurface maximum becomes apparent in $|U_0|$. Figure 11a depicts the variation in $|p_0|$ with depth for different internal friction values, representing a highly friction case ($A_v^*=10^{-1}$ m^2 s^{-1} or $St=3.09$), a moderately frictional case ($A_v^*=10^{-2}$ m^2 s^{-1} or $St=0.31$) and a weakly frictional case ($A_v^*=10^{-3}$ m^2 s^{-1} or $St=0.03$). The moderately and weakly frictional cases show a subsurface maximum for $|p_0|$, just as $|U_0|$. As mentioned above, similar results were found in *Prandle* [1982] and *Chen and de Swart* [2016].

Maxima in the M_2 tidal current amplitude were also found under reduced friction at the lateral boundaries of the basin, near the surface (Figure 7). To determine why there are maxima at the lateral boundaries, the solution for the M_2 tidal velocity (equation (30)) and water level (equation (36)) must be examined more closely for a fixed along-channel location (x^*). In the case of weak internal friction ($A_v^*\to 0$), p_0 (equation (31)) approaches 1 in the water column, except in the thin frictional boundary layer near the bottom. Hence, the equation for κ (equation (37)) reduces to, $\kappa=\omega^*/\sqrt{g^*h^*}$. Since $p_0\to 1$, the M_2 along-channel velocity amplitude (equation (30)) becomes $U_0=-ig^*/\omega^*\, dN_0/dx^*$ and two regimes arise from the wavenumber δ (equation (37) and contained in the solution for N_0), being real or complex. First, $\kappa^2 L_b^{*2}>1/4$ is satisfied for

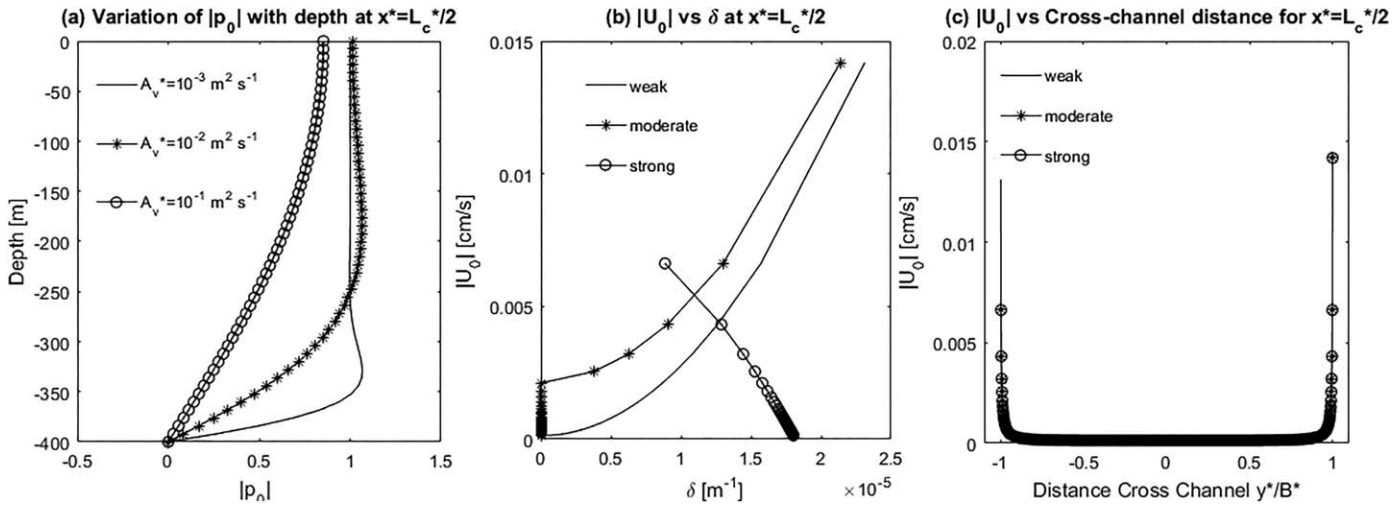

Figure 11. (a) Variation of $|p_0|$ (equation (31)) with depth at $x^*=L_c^*/2$ and $y^*/B^*=0$ for vertical eddy viscosity values of $A_v^*=10^{-3}$ m^2 s^{-1} (weak friction), $A_v^*=10^{-2}$ m^2 s^{-1} (moderate friction), and $A_v^*=10^{-1}$ m^2 s^{-1} (strong friction). (b) The M2 tidal velocity amplitude $|U_0|$ as a function of δ for a fixed along-channel location ($x^*=L_c^*/2$) and weak ($L_b^*=4L_c^*$ or $\mu=0.25$), moderate ($L_b^*=L_c^*$ or $\mu=1$), and strong ($L_b^*=L_c^*/2$ or $\mu=2$) width convergence strengths. (c) The M2 tidal velocity amplitude $|U_0|$ at $x^*=L_c^*/2$ as a function of cross-channel distance, y^*/B^* for varying width convergence strengths (same as those in Figure 11a). Both figures are plotting the tidal velocity amplitude for the weak internal friction regime $A_v^*=10^{-3}$ m^2 s^{-1} ($St=0.031$).

weak to moderate width convergence ($L_b^* \geq L_c^*$ or $\mu \leq 1$) and ensures that δ is real. The second regime is satisfied when $\kappa^2 L_b^{*2} < 1/4$, implying that δ is complex. This second regime is satisfied for strong width convergence cases ($L_b^* < L_c^*$ or $\mu > 1$).

For the first case, $\kappa^2 L_b^{*2} > 1/4$, it is guaranteed that $\delta=\sqrt{4\kappa^2-\frac{1}{L_b^{*2}}}$ is real. This implies that the equation governing the M_2 water level N_0 (equation (36)) is also real and behaves as a standing wave. This is also seen in the phase difference between the water level and velocity ($\phi_{N0}-\phi_{U0}$) when friction is weak ($St=0.031$ or $A_v^*=10^{-3}$ m^2 s^{-1}; Figure 5a). In this regime, δ decreases monotonically with increasing h^*. Therefore, for a fixed along-channel location (x^*), $|U_0|$ will be increasing with increasing δ if it has a maximum for minimum h^*. Figure 11b shows this to be the case for the along-channel location $x^*=L_c^*/2$. Further, $|U_0|$ is shown to increase at the lateral boundaries when in this regime (Figure 11c). When width convergence is strong, we enter into the second regime where $\kappa^2 L_b^{*2} < 1/4$. This requirement implies that δ is complex and increases as h^* increases, conversely to the first case. Since δ is complex, so is the solution for the water level N_0, implying that it is no longer a standing wave. In particular, we see in Figure 5c that the phase difference between N_0 and U_0 resembles that of a progressive wave. In this regime $|U_0|$ for fixed x^* will decrease with increasing δ if it is maximum for minimum h^*, which is shown in Figures 11b and 11c.

The lateral distribution of tidal hydrodynamics can be influenced by Coriolis forcing (equation (32)) [*Winant*, 2007]. Results showed that lateral flows were negligible during slack tides when Coriolis forcing was removed from the model equations, despite the value of the vertical eddy viscosity (not shown). When Coriolis forcing was included the largest lateral flows over the tide cycle were found during slack tides when friction was moderate ($A_v^*=10^{-3}$ to 10^{-2} m^2 s^{-1}; Figures 8 and 9). As this was not one of the main objectives of this study, it will not be discussed further.

4.2. Proof-Of-Concept: Model and Data Comparison in Reloncavi Fjord

The model geometry was simplified to an elongated, funnel-shaped basin, from that of the actual, complex channel geometry (Figure 2). But as with all analytical models, this is a necessary step to obtain solutions. Many analytical models that assumed simplified basins produced reliable flow properties in estuaries [*Ianniello*, 1977, 1979; *Friedrichs and Aubrey*, 1994; *Winant*, 2007; *Chernetsky et al.*, 2010; *Waterhouse et al.*, 2010].

Reloncavi Fjord features a shallow stratified layer at the surface of the fjord that varies in strength and thickness depending on river discharge. For example, *Valle-Levinson et al.* [2007] found a small (<4 m thick) buoyant layer in Reloncavi Fjord in both March 2002 and May 2004. This layer represents ~1% of the total

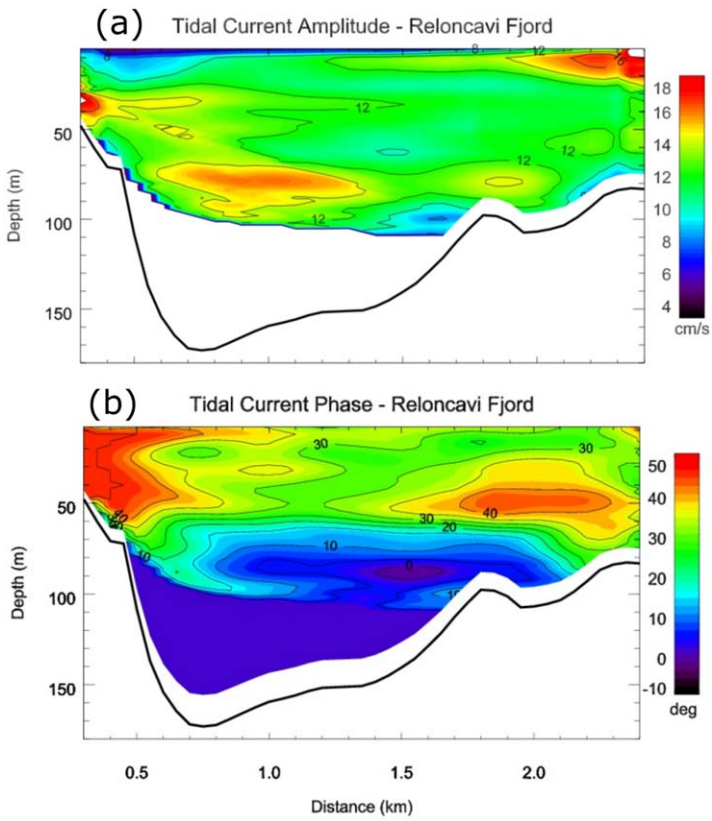

Figure 12. M_2 tidal current (a) amplitude and (b) phase in the middle of the channel ($x^*=27$ km) as a function of cross-channel distance and depth in Reloncavi Fjord. These data are from the ADCP transect performed in May 2004.

depth at the deepest portion of the fjord (400 m deep) and ~2% of the depth at the location of the underway current velocity measurements collected in May 2004 (data compared to model results in this study). Below the buoyant layer, the underlying water was homogeneous, as is typically the case in fjords [*Farmer and Freeland*, 1983; *Inall and Gillibrand*, 2010; *Pantoja et al.*, 2010; *Ross et al.*, 2014]. Therefore, assuming homogeneous conditions for the tide (no density gradients) is reasonable. This is particularly the case for Reloncavi Fjord, as it does not feature shallow sills (or moraines) [*Valle-Levinson et al.*, 2007].

Model results were compared qualitatively to underway velocity profiles collected throughout a semidiurnal tidal cycle in Reloncavi Fjord in 2004 (Figure 2). These data were presented in *Valle-Levinson et al.* [2007]. The tidal current amplitude showed strongest velocities (~0.2 m s^{-1}) near the lateral boundaries (cross-channel position between 0.4 and 0.5 km and 2 and 2.4 km) near the surface (10–50 m depth) (Figure 12a). In addition, maximum velocities were found subsurface near the center of the channel (0.6–2 km cross-fjord and ~80 m depth; Figure 12a). This pattern was qualitatively similar to the model output when $St<0.1$ (Figures 7c and 12a). In addition, when width convergence and friction were weak ($L_b^*=4L_c^*$ i.e., $\mu=0.25$ and $St=0.03$), model results showed along-channel velocity magnitude maximum values similar to those found in Reloncavi Fjord (~0.2 m s^{-2}; Figures 7c and 12a). The tidal current phase in Reloncavi Fjord showed a similar pattern to model output when $St<$ 0.1 (Figures 7f and 12b). In particular, the model output showed a bottom to surface phase change of ~60°, and weaker lateral change in the upper water column (~30° from the model boundary to the center of the channel). The observations showed similar results, with a sharp phase change of ~50° from bottom to surface and a slight variation in phase laterally (~20°).

The lateral variation of along-fjord flows found in Reloncavi Fjord (Figure 12) was assumed to be the result of centrifugal accelerations underneath the surface buoyant layer [e.g., *Seim et al.*, 2002; *Lacy et al.*, 2003] or of streamwise bathymetric changes that cause form drag [*Edwards et al.*, 2004; *Valle-Levinson et al.*, 2007]. This study reveals that lateral variations of along-channel flow in Reloncavi Fjord are also a consequence of tidal flow in a channel with $St\sim0.1$ (indicating small frictional influence, $A_v^*\sim10^{-3}$ m^2 s^{-1}) and weak width convergence ($L_b^*=4L_c^*$ or $\mu=0.25$).

Conditions for which the model domain transitions from frictionally influenced to frictionless are shown in Figure 10, which imply that this model is applicable to deep and narrow basins with varying degrees of friction. Other examples of deep-silled fjords for which this model is relevant are Martinez Channel and Puyuhuapi Channel in Chilean Patagonia [*Ross et al.*, 2015; *Schneider et al.*, 2014]. Unfortunately, there are no data to compare with the model in these systems, which accentuates the value of the model. Also, this model is applicable to other systems (not just fjords) where there are no prominent sills. In particular, it can

be implemented in deep, narrow and well-mixed systems with diverse frictional conditions (dynamically deep or shallow) by varying the Stokes number such as systems in the Gulf of Maine [*Hulburt*, 1968].

4.3. Model Limitations

This model was used in order to gain insight into tidal flow in fjord-like systems with deep (or no) sills. As a consequence, several simplifications to the model make it suspect for comparison to natural fjords and estuaries. First, the model does not apply to fjords with shallow sills. This implies that the model cannot capture the loss of tidal energy through tidal jets or tidal conversion that occurs near a sill, as was studied in *Stigebrandt and Aure* [1989], and references therein. Properties that are not taken into account in this model include density gradients, channel curvature, and along-channel depth variations. In particular, Reloncavi Fjord features a bend to the northeast near the midreaches of the channel (Figure 2), which was thought to increase along-channel tidal flow on the eastern shoal (Figure 12) [*Valle-Levinson et al*., 2007]. This flow feature was not captured by the model because of its simplified geometry. Also, the vertical eddy viscosity was chosen to be constant in order to simplify the analytical solution. More accurate results could result from a depth varying vertical eddy viscosity profile [*Burchard and Hetland*, 2010; *Chen and de Swart*, 2016]. However, despite the simplifications, model results reproduced the essence of observations.

5. Conclusions

This study investigated the effect of channel width convergence and friction on semidiurnal sea surface elevation and tidal flow in a deep and narrow basin. In particular, it investigated how these parameters modify the location of along-channel velocity maxima. This was done with a three-dimensional analytical model that included width convergence, Coriolis. and arbitrary cross-channel bathymetry.

As width convergence strengthened (values of L_b^* decreased), the sea surface amplitude increased along the basin. However, considering both friction and width convergence strength, values of L_b^* ($2L_c^*/3 < L_b^* < L_c^*$ or $1 < \mu < 1.5$) and Stokes number ($St < 0.03$) showed a maximum in sea surface amplitude ($\sim$0.5 m) at the head of the basin. Cross-channel variations of along-channel tidal flow showed typical open channel flow (velocity maximum in the center of the channel at the surface) under large Stokes numbers ($St > 0.1$). However, when $St < 0.1$, the along-channel velocity maxima became submerged and showed largest values near the lateral boundaries. The maxima at the lateral boundaries were explained by a simplification of the complex wavenumber under weak friction leading to an increase in M_2 along-channel tidal amplitude with decreasing depth. The subsurface velocity maximum occurred because the frictional boundary layer was much less than the water depth, indicating that the fjord-like basin was dynamically deep, leading to a submerged tidal velocity maximum.

Model results of M_2 tidal amplitude were compared to observations from Reloncavi Fjord in Chilean Patagonia. Results showed velocity maxima subsurface and at the lateral boundaries near the surface. This indicates that the model can reproduce the tidal current structure in fjord-like basins.

Acknowledgments
This work is part of the research program "Impact of climate change and human intervention on hydrodynamics and environmental conditions in the Ems-Dollart estuary: an integrated data-modeling approach." This project is financed by the Bundesministerium fur Bildung und Forschung (BMBF) and by the Netherlands Organization for Scientific Research (NWO), as part of the international Wadden Sea Program (GEORISK project). Data in Reloncavi Fjord were collected with funding from the Instituto Tecnolgico del Salmon (INTESAL) in Chile and by the Ncleo Milenio FORECOS in Chile. Assistance in the field of D. Soto, R. Sanay, N. Sarkar, J. Soto, J. L. Blanco, D. Salas, H. Perales, I. Arismendi, C. Leal, M. Castillo, and V. Barrera is greatly appreciated. M. Cceres kindly provided bathymetric data of the fjord. A.V.L. was supported by NSF grant OCE-1332718. The data and model code are available at the following link: dataverse.acg.maine.edu/dvn/dv/ECOlab/faces/study/StudyPage.xhtml?globalId=hdl:TEST/10139.

References

Burchard, H., and R. D. Hetland (2010), Quantifying the contributions of tidal straining and gravitational circulation to residual circulation in periodically stratified tidal estuaries, *J. Phys. Oceanogr.*, *40*, 1243–1262, doi:10.1175/2010JPO4270.1.

Cáceres, M., A. Valle-Levinson, H. H. Sepúlveda, and K. Holderied (2002), Transverse variability of flow and density in a Chilean fjord, *Cont. Shelf Res.*, *22*(11–13), 1683–1698, doi:10.1016/S0278-4343(02)00032-8.

Chen, W., and H. E. de Swart (2016), Dynamic links between shape of the eddy viscosity profile and the vertical structure of tidal current amplitude in bays and estuaries, *Ocean Dyn.*, *66*(3), 299–312, doi:10.1007/s10236-015-0919-6.

Chernetsky, A. S., H. M. Schuttelaars, and S. A. Talke (2010), The effect of tidal asymmetry and temporal settling lag on sediment trapping in tidal estuaries, *Ocean Dyn.*, *60*, 1219–1241, doi:10.1007/s10236-010-0329-8.

Csanady, G. T. (1982), Circulation in the coastal ocean, in *Environmental Fluid Mechanics*, vol. 2, D. Reidel Publishing Company, Dordrecht, Holland.

Dyer, K. R. (1997), *Estuaries: A Physical Introduction*, John Wiley & Sons, New York, N. Y.

Edwards, K. A., P. MacCready, J. N. Moum, G. Pawlak, J. M. Klymak, and A. Perlin (2004), Form drag and mixing due to tidal flow past a sharp point, *J. Phys. Oceanogr.*, *34*, 1297–1312, doi:10.1175/1520-0485(2004)034<1297:FDAMDT>2.0.CO;2.

Ensing, E., H. E. deSwart, and H. M. Schuttelaars (2015), Sensitivity of tidal motion in well-mixed estuaries to cross-sectional shape, deepening, and sea level rise, *Ocean Dyn.*, *65*, 933–950.

Farmer, D. M., and H. J. Freeland (1983), The physical oceanography of fjords, *Prog. Oceanogr.*, *12*, 147–220.

Folger, D. W., R. H. Meade, B. F. Jones, and R. L. Cory (1972), Sediments and waters of Somes Sound, a fjordlike estuary in Maine, *Limnol. Oceanogr.*, *17*(3), 394–402.

Friedrichs, C. T., and D. G. Aubrey (1994), Tidal propagation in strongly convergent channels, *J. Geophys. Res.*, *99*, 3321–3336.

Friedrichs, C. T., and J. M. Hamrick (1996), Effects of channel geometry on cross sectional variations in along channel velocity in partially stratified estuaries, in *Buoyancy Effects on Coastal and Estuarine Dynamics*, edited by D. G. Aubrey and C. T. Friedrichs, American Geophysical Union, Washington, D. C., doi:10.1029/CE053p0283.

Huijts, K. M. H., H. Schuttelaars, H. E. de Swart, and A. Valle-Levinson (2006), Lateral entrapment of sediment in tidal estuaries: An idealized model study, *J. Geophys. Res.*, *111*, C12016, doi:10.1029/2006JC003615.

Huijts, K. M. H., H. E. de Swart, G. P. Schramkowski, and H. Schuttelaars (2011), Transverse structure of tidal and residual flow and sediment concentration in estuaries, *Ocean Dyn.*, *61*(8), 1067–1091, doi:10.1007/s10236-011-0414-7.

Hulburt, E. M. (1968), Stratification and mixing in coastal waters of the western Gulf of Maine during summer, *J. Fish. Res. Board Can.*, *25*(12), 2609–2621.

Ianniello, J. P. (1977), Tidally induced residual current in estuaries of constant breadth and depth, *J. Geophys. Res.*, *35*, 755–786.

Inall, M. E., and P. A. Gillibrand (2010), The physics of mid-latitude fjords: A review, *Geol. Soc. Spec. Publ.*, *344*, 17–33, doi:10.1144/SP344.3.

Lacy, J. R., M. T. Stacey, J. R. Burau, and S. G. Monismith (2003), Interaction of lateral baroclinic forcing and turbulence in an estuary, *J. Geophys. Res.*, *108*(C3), 3089, doi:10.1029/2002JC001392.

Lamb, H. (1932), *Hydrodynamics*, 6th ed., Cambridge Univ. Press, Cambridge, U. K.

Murray, A. B. (2003), Contrasting the goals, strategies, and predictions associated with simplified numerical models and detailed simulations, in *Prediction in Geomorphology, Geophys. Monogr. Ser.*, edited by P. R. Wilcock and R. M. Iverson, vol. 135, AGU, Washington, D. C., doi:10.1029/135GM11.

Officer, C. B. (1976), *Physical Oceanography of Estuaries (and Associated Coastal Waters)*, John Wiley & Sons, New York, N. Y.

Pantoja, S., J. L. Iriarte, and G. Daneri (2010), Oceanography of the Chilean Patagonia, *Cont. Shelf Res.*, *31*(3–4), 149–153.

Pond, S., and G. L. Pickard (1983), *Introductory Dynamical Oceanography*, 2nd ed., pp. 44–62, Elsevier, Oxford, U. K.

Pope, S. B. (2000), *Turbulent Flows*, Cambridge Univ. Press, Cambridge, Mass.

Prandle, D. (1982), The vertical structure of tidal currents and other oscillatory flows, *Cont. Shelf Res.*, *1*(2), 191–207.

Ross, L., I. Pérez-Santos, W. Schneider, and A. Valle-Levinson (2014), Semidiurnal internal tides in a Patagonian fjord, *Prog. Oceanography*, *129*, 19–34, doi:10.1016/j.pocean.2014.03.006.

Salcedo-Castro, J., D. Bourgault, and B. deYoung (2011), Circulation induced by subglacial discharge in galcial fjords: Results from idealized numerical simulations, *Cont. Shelf Res.*, *31*, 1396–1406.

Schneider, W., I. Pérez-Santos, L. Ross, L. Bravo, R. Seguel, and F. Hernández (2014), On the hydrography of Puyuhuapi Channel, Chilean Patagonia, *Prog. Oceanogr.*, *129*, 8–18, doi:10.1016/j.pocean.2014.03.007.

Seim, H. E., J. O. Blanton, T. Gross (2002), Direct stress measurements in a shallow, sinuous estuary, *Cont. Shelf Res.*, *22*(11–13), 1565–1578, doi:10.1016/S0278-4343(02)00029-8.

Sorenson, R. M. (2006), *Basic Coastal Engineering*, pp. 115–117, Springer, New York.

Stigebrandt, A., and J. Aure (1989), Vertical mixing in basin waters of fjords, *Am. Meteorol. Soc.*, *19*, 917–926.

Sutherland, D. A., F. Straneo, and R. S. Pickart (2014), Characteristics and dynamics of two major Greenland glacial fjords, *J. Geophys. Res.*, *119*, 3767–3791, doi:10.1002/2013JC009786.

Valle-Levinson, A., N. Sarkar, R. Sanay, D. Soto, and J. León (2007), Spatial structure of hydrography and flow in a Chilean Fjord, Estuario Reloncaví, *Estuaries Coasts*, *30*(1), 113–126.

Valle-Levinson, A. (2010), Definition and classification of estuaries, in *Contemporary Issues in Estuarine Physics*, edited by A. Valle-Levinson, pp. 1–11, Cambridge Univ. Press, New York.

Valle-Levinson, A., M. A. Caceres, and O. Pizarro (2014), Variations of tidally driven three-layer residual circulation in fjords, *Ocean Dyn.*, *64*(3), 459–469, doi:10.1007/s10236-014-0694-9.

Vreugdenhil, C. B. (1994), Shallow-water flows, in *Numerical Methods for Shallow-Water Flow, Water Science and Technology Library*, vol. 13, Springer, Dordrecht, The Netherlands, doi:10.1007/978-94-015-8354-1_1.

Waterhouse, A. F., A. Valle-Levinson, and C. D. Winant (2010), Tides in a system of connected estuaries, *J. Phys. Oceanogr.*, *41*, 946–959.

Winant, C. D. (2007), Three-dimensional tidal flow in an elongated, rotating basin, *J. Phys. Oceanogr.*, *37*, 2345–2362, doi:10.1175/JPO3122.1.

Winant, C. D. (2008), Three dimensional residual tidal circulation in an elongated, rotating basin, *J. Phys. Oceanogr.*, *38*, 1278–1295, doi:10.1175/2007JPO3819.1.